

## FUELCELL2008-65027

### NUMERICAL SIMULATION OF ELECTROCHEMICAL REACTION IN RECONSTRUCTED THREE-DIMENSIONAL LSM/YSZ COMPOSITE CATHODE

Tadahiro Nakagawa, Naoki Shikazono and Nobuhide Kasagi

The University of Tokyo  
Department of Mechanical Engineering  
Hongo 7-3-1, Bunkyo-ku, Tokyo, 113-8656, Japan

#### ABSTRACT

In the present study, a novel computational scheme for the assessment of the activation polarization of LSM/YSZ composite cathodes is proposed. The scheme consists of modeling techniques of three-dimensional microstructures and an evaluation method of electrochemical characteristics.

Two modeling techniques of microstructures are employed, i.e. the stochastic reconstruction (SR) method and the random packing model (RPM). In the SR method, the 3-D structure is reconstructed statistically from the two-point correlation function of the cross-sectional image of SEM-EDX. In RPM, on the other hand, spherical LSM and YSZ particles are randomly packed in the computational domain. This model is mainly used for the parametric survey, because control parameters used in the model have good correspondence to the parameters used in the actual cell manufacturing process. The lattice Boltzmann method coupled with the Butler-Volmer equation is employed for the detailed assessment of the electrochemical characteristics inside the constructed 3-D cathode microstructures. The oxygen diffusion and the electronic and ionic conductions are calculated simultaneously, and coupled with the charge transfer at the three-phase boundary (TPB) using the Butler-Volmer equation.

As a result, potential, polarization and current density distributions are fully investigated. The results from the SR method reveal that the cathode sintered at 1150 °C shows the smaller overpotential than the cathodes sintered at 1200 and 1250 °C. The RPM results show that particle diameter and its standard deviation as well as volume fraction of species have large effects on the cathode performance.

*Keywords:* Solid oxide fuel cell, Lattice Boltzmann simulation, Cathode microstructure, Three-phase boundary

#### 1. INTRODUCTION

The improvements in the experimental and the numerical techniques lead to more detail analyses of the electrode microstructures of solid oxide fuel cells (SOFCs). Recently, 3-D observation of anode using a focused ion beam-scanning electron microscope (FIB-SEM) was demonstrated by Wilson *et al.* [1]. Detailed information on anode microstructures can be obtained from direct measurement, but it requires long processing time with very expensive apparatus. Koyama *et al.* [2] performed a parameter survey of an anode microstructure using a random packing model. The random packing models have large advantages because the control parameters are similar to the parameters used in the actual manufacturing processes. However, the validity of the assumption of sphere particles remains unclear.

On the other hand, Suzue *et al.* [3] developed a new scheme to evaluate the comprehensive polarization characteristics inside the three-dimensional microstructure of SOFC anodes. The stochastic reconstruction (SR) method of Yeong and Torquato [4] was employed to reconstruct the microstructures. The diffusion, ionic and electric conductions are solved simultaneously by the lattice Boltzmann method (LBM). Recently, several researchers, e.g., Asinari *et al.* [5] and Joshi *et al.* [6] are reported to investigate the effects of 3-D anode microstructures. However, few studies deal with cathodes because the microstructures of SOFC cathodes are relatively finer than that of anodes, and also because the differentiation of phases is considerably difficult for LSM/YSZ composites with secondary electron images. It is well known that cathode polarization comes to be dominant at intermediate and low temperatures. Thus, detailed 3-D investigations of the composite cathodes are strongly required.

Therefore, the objective of this study is to propose and assess the 3-D numerical simulation tool for the LSM/YSZ composite cathodes to investigate the relationship between

cathode microstructures and its polarization characteristics. The microstructures are reconstructed using the stochastic reconstruction (SR) method and the random packing model (RPM). Furthermore, the polarization characteristics of composite cathodes are assessed using the lattice Boltzmann method.

## 2. MICROSTRUCTURE MODELING

### 2.1 SAMPLE PREPARATION

Anode-support tubular SOFCs (Sakamoto *et al.* [7]) are used as test samples. The LSM-YSZ (50/50 wt.%) composite cathode is employed, and the thickness of the dip-coated cathode layer is 5-10  $\mu\text{m}$ . The sintering temperature is varied to change its microstructure. High sintering temperature is preferred to get good connectivity between solid particles. However, too high sintering temperature deteriorates the cathode performance due to large sintered particles with the small TPB length. In this study, the cathode is sintered at temperatures of 1150, 1200 and 1250  $^{\circ}\text{C}$ .

It is difficult to obtain clear images of composite cathode microstructures with a conventional secondary electron SEM. In this study, a scanning electron microscope with energy and angle selective backscattered detector (Carl Zeiss Ultra 55) and an energy dispersive X-ray spectroscopy (Thermo ELECTRON Corp., NSS300) are employed in order to acquire high-resolution images. It becomes possible to obtain very high-resolution images with the extremely low acceleration voltage SEM. The pores were distinguished from the SEM image, and LSM and YSZ phases were separated from the EDX image (Fig. 1). Images were processed so as to obtain clear boundaries of phases as shown in Fig. 3.

In the present study, two approaches are employed for reconstructing 3-dimensional microstructures from the processed 2-D images, i.e., the stochastic reconstruction (SR) method and the random packing model (RPM). Each of them will be explained in the following sections.

### 2.2 STOCHASTIC RECONSTRUCTION

In the SR method, a 3-D structure is reconstructed from the processed 2-D image of a cathode microstructure. The two-point correlation function  $R_{ij}$  between phases  $i$  and  $j$  ( $i, j=0-2$ ) in an isotropic structure is defined as follows:

$$R_{ij}(r) = \frac{\overline{\delta(Z(\mathbf{x}),i) \cdot \delta(Z(\mathbf{x}+\mathbf{r}),i)}}{\overline{\delta(Z(\mathbf{x}),i)}}, \quad (1)$$

where  $\delta(i, j)$  represents the Kronecker's delta function. And the phase function  $Z(\mathbf{x})$  is defined as follows:

$$Z(\mathbf{x}) = \begin{cases} 0 & \text{(pore, black)} \\ 1 & \text{(YSZ, gray)} \\ 2 & \text{(LSM, white)} \end{cases} \quad (2)$$

The two-point correlation function represents the statistic characteristics of the microstructure. It stands for the probability that a pixel is phase  $i$  when the other pixel in distance  $r$  is phase  $j$ . Since the cathode layer thickness is less than 10  $\mu\text{m}$ , the sampling domain was not enough to obtain well-converged 2-point correlation functions. Therefore, averaged 2-point correlation curves functions are obtained from 2~4 images are used as reference s for the reconstruction.

The 3-D microstructure of cathode is reconstructed stochastically by the iterative scheme based on the reference functions (Suzue *et al.* [3], Young and Torquato [4]). The grid size  $l$  is set as 0.0596  $\mu\text{m}$  in each direction. Periodic boundary conditions are imposed in all directions. At first, each voxel is assigned randomly with three phases according to their volume fraction. Then, reconstruction is performed to minimize the evaluation function  $E$  defined as follows:

$$E = \sum_{i,j} \int \left\{ R_{ij}^{3D}(r) - R_{ij}^{2D}(r) \right\}^2 dr, \quad (3)$$

where  $R_{ij}^{3D}$  is the reconstructed two-point correlation and  $R_{ij}^{2D}$  is the two point correlation of the original 2-D image.

The integral  $dr$  is performed only in the directions of the principal axes in order to reduce the computational cost. The interval of integration is set as 1.78  $\mu\text{m}$ . Starting from a random configuration, two voxels of different phases are exchanged at each integration step only when the evaluation function  $E$  decreases. The reconstruction required more than 100 Monte Carlo steps before the evaluation function gets to be constant. As shown in Fig. 2, the two-point correlation curves of reconstructed 3-D structure and the original 2-D image show good agreement. The residuals of Eq. (3) are less than 2.5 %. The 3-D microstructures with different sintering temperatures are reconstructed successfully as shown in Fig. 4.

### 2.3 RANDOM PACKING MODEL

The other reconstruction approach is the random packing model (RPM). While SR is aimed to reproduce microstructures as realistic as possible, RPM is suitable to control the structural parameters, which are in close relation with the parameters used in the actual manufacturing process. In RPM, spherical particles are packed to construct structures (Koyama *et al.* [2]). As shown in Fig. 5, particle diameter  $d$ , volume ratio of ionic conductor  $\varphi_{io}$ , the overlap ratio  $\alpha$  and the standard deviation of particle diameter  $\sigma$  are employed as structural parameters.

The overlap ratio  $\alpha$  is defined as the ratio of the length between the centers of the sintered particles to the sum of the original radii of two particles. For example, if  $\alpha$  is small two particles are sintered and connected closely, which leads to larger contact angle as shown in Fig. 5 (c). In this study, the overlap ratios between particles of the same phase and those between different phases are changed in order to imitate realistic

structures. Normal distribution is assumed for the particle diameter distribution.

Figure 6 shows the numerical procedure of RPM, which is basically the same as Koyama *et al.* [2]. First,  $I_N$  individual spherical particles are prepared. The phases (LSM or YSZ) and their diameter distributions are determined according to the given parameters. Particles are packed randomly in the computational domain with the given overlap ratio in descending order. If a packed particle doesn't satisfy the input parameters, another place is tried. This process is iterated until all particles are packed. The 3-D structures are built with much smaller computational cost than SR method. The 2-point correlation curves and the schematic of the reconstructed PRM structures of a cathode sintered at 1150 °C are shown in Figs. 7 and 8, respectively. Good agreement of two point correlations with the 2-D image is obtained. Totally, 9 different microstructures are reconstructed by varying particle diameter  $d$ , standard deviation of particle diameter  $\sigma$ , the volume ratio of YSZ  $\varphi_{io}$ , and the overlap ratio  $\alpha$ .

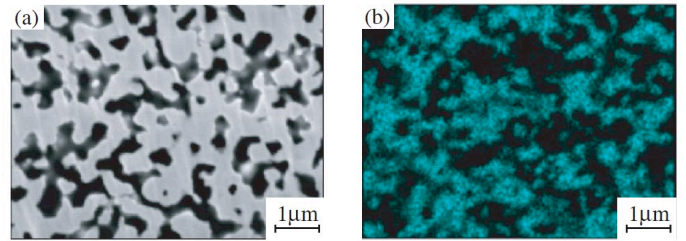


Fig. 1 (a) SEM and (b) EDX images of cathode microstructure sintered at 1150 °C.

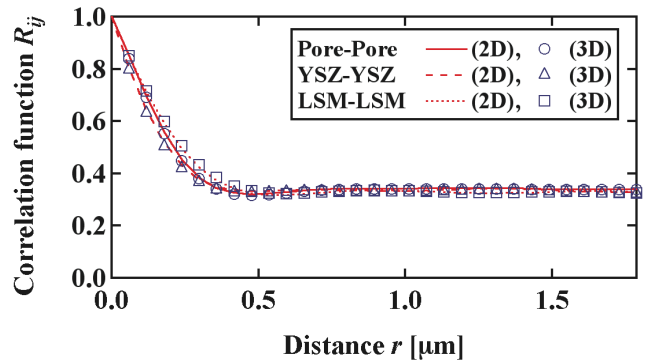


Fig. 2 Two-point correlation functions of cathode sintered at 1150 °C.

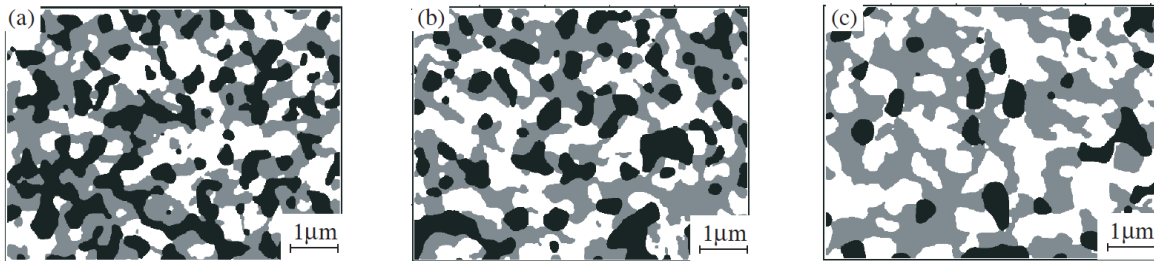


Fig. 3 Phase separated image of cathode sintered at (a) 1150 °C, (b) 1200 °C and (c) 1250 °C. Black phase is pore, gray phase is YSZ, and white phase is LSM.

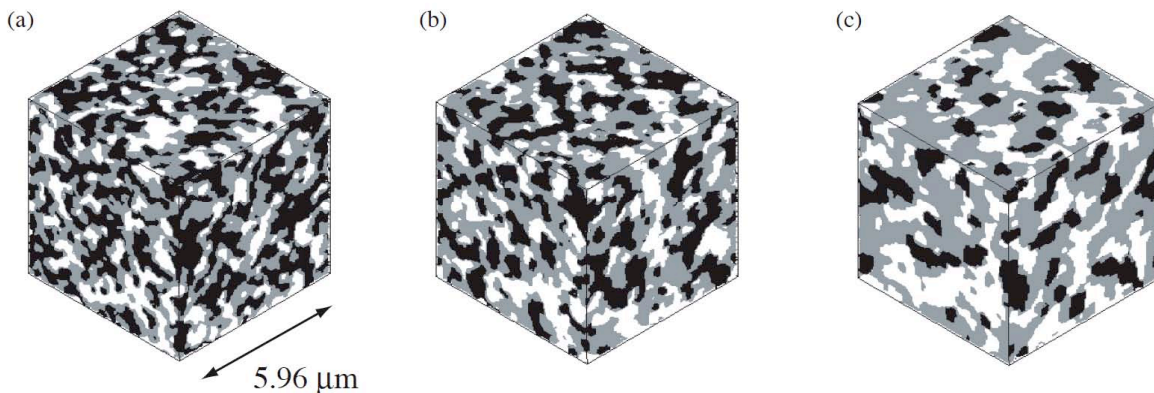


Fig. 4 Reconstructed structures of cathode sintered at (a) 1150 °C, (b) 1200 °C and (c) 1250 °C. Black phase is pore, gray phase is YSZ, and white phase is LSM.

### 3. ELECTROCHEMICAL ANALYSIS

#### 3.1 COMPUTATIONAL DOMAIN

The cathode polarizations of reconstructed structures are calculated from 3-D detailed numerical simulations. The schematic of the computational domain is shown in Fig. 9. In order to model the actual cathode operating condition, current collector (LSM) and electrolyte (YSZ) layers are added to the both ends of the computational domain. The thicknesses of the current collector and the electrolyte layers are  $0.596 \mu\text{m}$  (10 grids) and  $1.192 \mu\text{m}$  (20 grids), respectively. Temperature and total pressure are assumed to be uniform. The simulation conditions are summarized in Table 1.

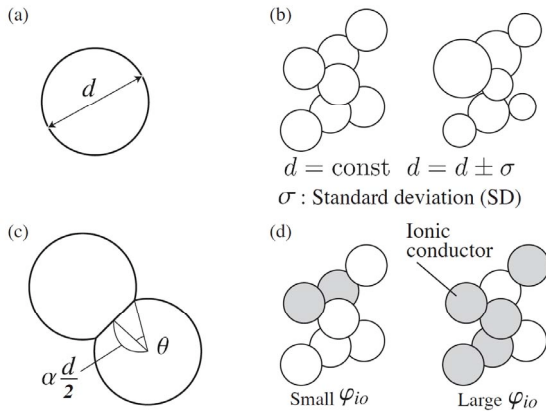


Fig. 5 Design parameters in RPM.

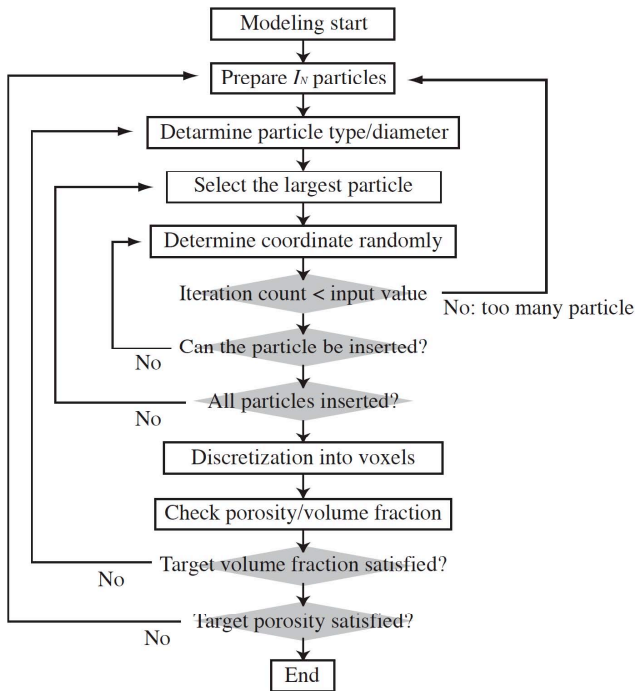


Fig. 6 Modeling procedure of RPM.

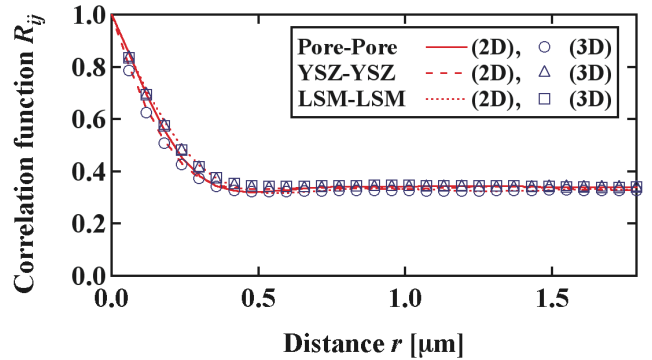


Fig. 7 Two-point correlation functions of cathode by RPM.

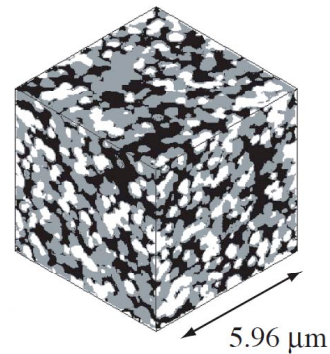


Fig. 8 Reconstructed microstructure by RPM.

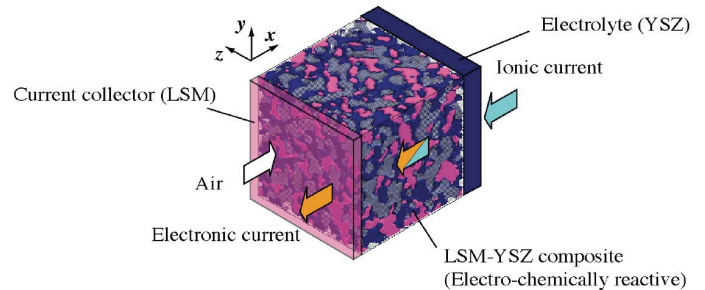


Fig. 9 Schematic of the computational domain.

Table 1 Operating conditions.

|                             |                                 |
|-----------------------------|---------------------------------|
| Temperature                 | 800 [ $^{\circ}\text{C}$ ]      |
| Current density             | 10000 [ $\text{A}/\text{m}^2$ ] |
| $\text{O}_2$ molar fraction | 0.21 [-]                        |

Constant and uniform current is assumed at the current collector and the electrolyte boundaries. The three-phase boundary (TPB) length is estimated to be 80 % of the value directly calculated from the cubic voxel perimeter of the digital structure. The total computational volume size is  $8.94 \mu\text{m}$  with 150 grids for SR structures, and  $5.96 \mu\text{m}$  with 100 grids for RPM structures. This is because accurate analysis is the main focus for SR, while RPM targets wide-range parametric survey.

### 3.2 GOVERNING EQUATIONS

According to Jeon *et al.* [12], LSM and YSZ are assumed to be the electronic and ionic conductor, respectively. The governing equations in pore, LSM and YSZ phases are the diffusion equation for the oxygen gas, and the charge transfer equations for electron and ion, which are written as follows:

$$\frac{\partial}{\partial x} \left( D \frac{\partial C}{\partial x} \right) = -\frac{1}{4F} i_{\text{reac}}, \quad (4)$$

$$\frac{\partial}{\partial x} \left( \sigma_{el} \frac{\partial \phi_{el}}{\partial x} \right) = i_{\text{reac}}, \quad (5)$$

$$\frac{\partial}{\partial x} \left( \sigma_{io} \frac{\partial \phi_{io}}{\partial x} \right) = -i_{\text{reac}}. \quad (6)$$

Here, RHSs in Eqs. (4)-(6) are the reaction production terms, and the local reaction current  $i_{\text{reac}}$  is calculated from the local potential around TPB. Assuming isobaric conditions, the counter diffusion of oxygen and nitrogen are solved by the extended Fick's law. And only the diffusion of oxygen is explicitly solved.

The charge transfer between the electronic and ionic conductors is solved by the Butler-Volmer equation (Costamagna *et al.* [8]):

$$i_{\text{reac}} = i_0 L_{\text{TPB}} \left\{ \exp\left(\theta_a \frac{F}{RT} \eta\right) - \exp\left(\theta_c \frac{F}{RT} \eta\right) \right\}, \quad (7)$$

$$\eta = \phi_{el} - \phi_{io}, \quad (8)$$

where  $L_{\text{TPB}}$  is the TPB length per unit volume and  $i_0$  stands for the lineal exchange current density:

$$i_0 = \gamma \cdot \left( \frac{p_{\text{O}_2}}{p_{\text{O}_2, \text{ref}}} \right)^{0.25} \cdot \exp\left(-\frac{E_A}{RT}\right). \quad (9)$$

The lineal exchange current density  $i_0$  is a function of oxygen partial pressure  $p_{\text{O}_2}$ , activation energy  $E_A$ , and temperature  $T$ . The constant  $\gamma$  is determined as 176.4 from the experimental data of Radhakrishnan *et al.* [10].

The diffusivity of oxygen is assumed to be constant and determined from Chan and Xia [11]. The electronic and the ionic conductivities are determined as follows (Jeon *et al.* [12]):

$$\sigma_{el} = 3.34 \times 10^4 \exp\left(-\frac{10300}{T}\right), \quad (10)$$

$$\sigma_{io} = \frac{8.855 \times 10^7}{T} \exp\left(\frac{1082.5}{T}\right). \quad (11)$$

### 3.3 COMPUTATIONAL METHOD

In this study, the lattice Boltzmann method (LBM) is employed to solve the diffusion equation (4) and the charge transfer equations (5) and (6), which are in the analogously same form. The boundary conditions can be easily set in LBM, and therefore LBM is suitable to solve the flow within complicated porous structures. Moreover, it is easy to introduce source term because LBM is based on the potential difference of fluid. Thus, LBM is considered to be very effective to solve the electrochemical process in the electrode.

The temporal changes of velocity distribution function  $f_i(\mathbf{x}, t)$  is solved in LBM using the lattice Boltzmann equation:

$$f_i(\mathbf{x} + \mathbf{c}_i \cdot \Delta t, t + \Delta t) = f_i(\mathbf{x}, t) - \frac{1}{\tau^*} [f_i(\mathbf{x}, t) - f_i^{eq}(\mathbf{x}, t)] + w_i \Delta t, \quad (12)$$

where  $\mathbf{c}_i$  is the lattice velocity,  $t$  is time and  $\tau^*$  is the relaxation coefficient. Subscript  $i$  stands for the vector component of the lattice velocity, and  $w_i$  is the reaction product per unit time. In this study, the relaxation coefficient is set as 0.99 [3]. D3Q6 ( $i=1-6$ ) model is employed in this study, because D3Q6 model is reliable enough for diffusion process without convection (Zeiser *et al.* [13], Suzue *et al.* [3]). No-flux boundary conditions are imposed on the boundary of each phase in the porous media by applying the halfway bounceback scheme.

Periodic boundary conditions are assumed in the spanwise ( $y$  and  $z$ ) directions. At the current collector surface, constant gas composition is assumed. Constant electronic and ionic current flux conditions are imposed on the current collector and electrolyte boundaries.

## 4. RESULTS AND DISCUSSION

### 4.1 EVALUATION CRITERIA OF ELECTRODE

The predicted overpotentials in the composite cathode are evaluated in this section. It is well known that the overpotential in the electrode is closely related to the microstructure of the electrode, i.e., three-phase boundary (TPB) density and effective conductivity. The effective diffusivity in the porous media  $D^{eff}$  and the normal diffusivity  $D$  are related as follows:

$$D^{eff} = \frac{\varepsilon}{\tau} D, \quad (13)$$

where  $\varepsilon$  is the porosity and  $\tau$  is the tortuosity factor of the diffusive path of oxygen. Analogously, the effective electronic and ionic conductivities can be expressed as follows:

$$\sigma_{el}^{eff} = \frac{\varepsilon_{el}}{\tau_{el}} \sigma_{el}, \quad (14)$$

$$\sigma_{io}^{eff} = \frac{\varepsilon_{io}}{\tau_{io}} \sigma_{io}, \quad (15)$$

where  $\sigma_{el}^{eff}$  and  $\sigma_{io}^{eff}$  are the effective electronic and ionic conductivities,  $\varepsilon_{el}$  and  $\varepsilon_{io}$  are the volume fractions of the electronic and ionic conductive media,  $\tau_{el}$  and  $\tau_{io}$  are the tortuosity factors of the electronic and ionic paths, respectively. These effective gaseous, electronic and ionic diffusivity/conductivities can be obtained only from the three-dimensional diffusion/conduction analyses. In LSM/YSZ cathodes, the ionic conduction in YSZ phase and the charge transfer at TPB are the major rate-determining processes of the whole electrochemical reaction, and will be discussed in detail in the following section.

To discuss the electrochemical characteristics of the electrode, Thiele modulus is introduced (Costamagna *et al.* [8]):

$$\Gamma = L \sqrt{\frac{i_0 L_{TPB} F (\theta_a + \theta_c)}{RT} \left( \frac{1}{\sigma_{el}} + \frac{1}{\sigma_{io}} \right)}. \quad (16)$$

Thiele modulus  $\Gamma$  represents the ratio of the ionic conduction resistance to the activation overpotential. When  $\Gamma$  is small ( $\Gamma < 0.3$ ), the conductive resistivity is relatively small enough and thus the overpotential within the electrode becomes nearly uniform. On the contrary, when  $\Gamma$  is large ( $\Gamma > 3$ ), conductive resistivity of the electrode is large so that the overpotential drop sharply near the electrode-electrolyte interface [8].

Thiele modulus is the measure for understanding how effectively the whole electrode is utilized from the structural and material property characteristics. Generally, the value of Thiele modulus around 3 provides the optimal electrode performance (Costamagna *et al.* [9]).

## 4.2 ELECTROCHEMICAL CHARACTERISTICS OF THE CATHODE MICROSTRUCTURES

The electrochemical characteristics of SR are investigated. Figure 10 shows the comparison between predicted overpotential of SR structures and the experimental results of the composite cathodes (Song *et al.* [14] and Kim *et al.* [15]). As shown in Fig. 10, the optimal sintering temperature is between 1100 and 1200 °C. Although the cathode composition and operating conditions are different, prediction shows nearly the same trend as the experimental data. Figure 11 shows the predicted TPB density and the effective ionic conductivity for microstructures with different sintering temperatures. TPB density decreases as sintering temperature increases, while effective ionic conductivity increases with sintering temperature. Thus, the overpotential is determined by the trade-off between the TPB density and the ionic conductivity.

Figure 12 shows the overpotential distribution inside the electrode. The overpotential drops steeply near the electrode-electrolyte interface for the 1150 °C sintered cathode. On the other hand, the overpotential of the 1250 °C sintered cathode shows more uniform distribution. This difference can be explained using Thiele modulus shown in Fig. 13. Thiele

modulus increases as the cathode sintering temperature is lowered, which means that 1150 °C sintered cathode is more electrochemically reactive than that sintered at 1250 °C.

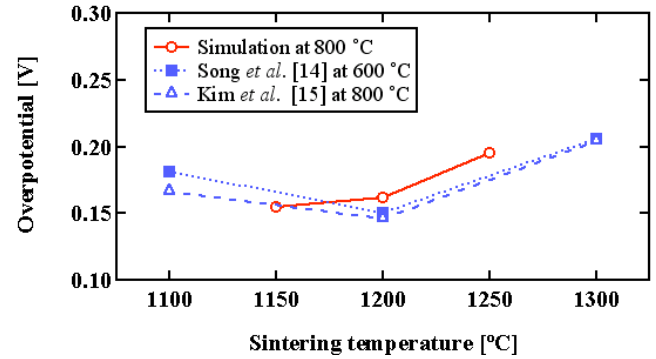


Fig. 10 Overpotential of cathode sintered at different temperatures by the SR method.

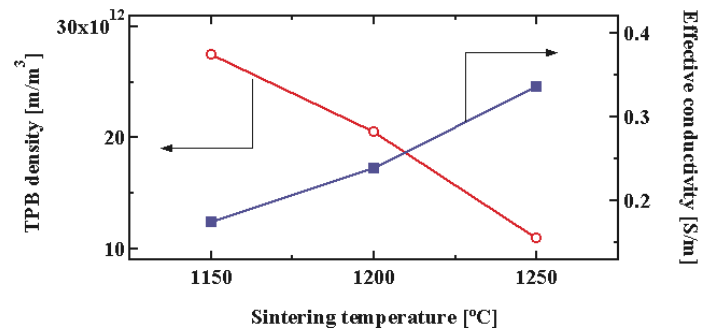


Fig. 11 Three-phase boundary density and effective ionic conductivity of cathode by SR method.

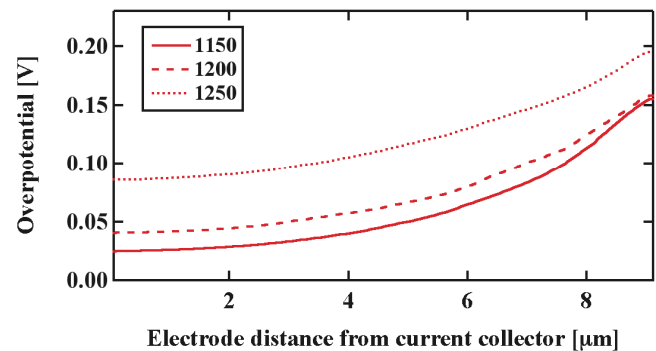


Fig. 12 Overpotential distribution inside the electrode.

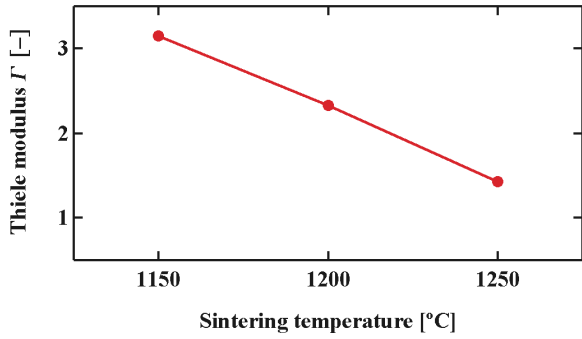


Fig. 13 Sintering temperature dependence of the Thiele modulus.

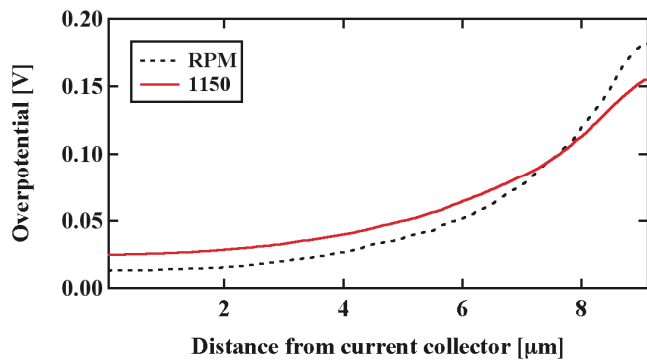


Fig. 14 Comparison of overpotential distributions from SR and RPM.

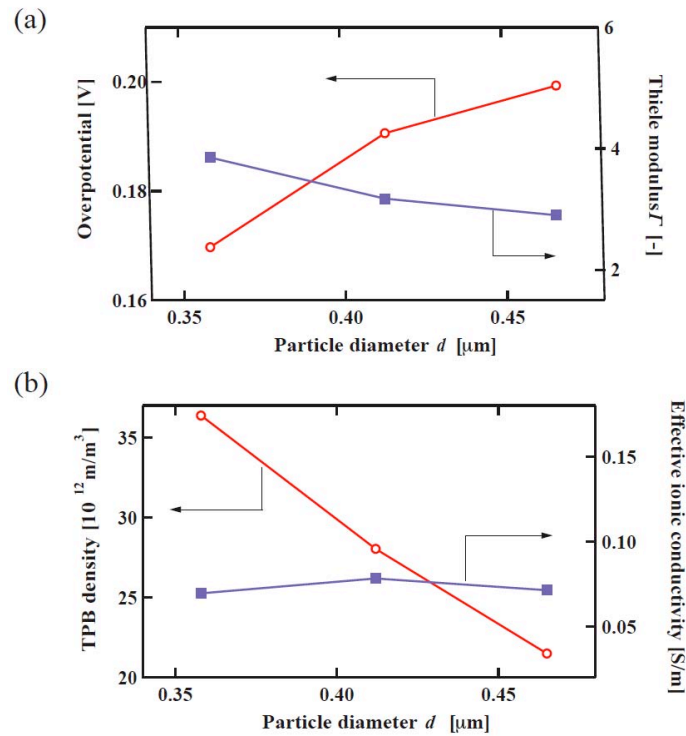


Fig. 15 The effects of particle diameter by RPM.

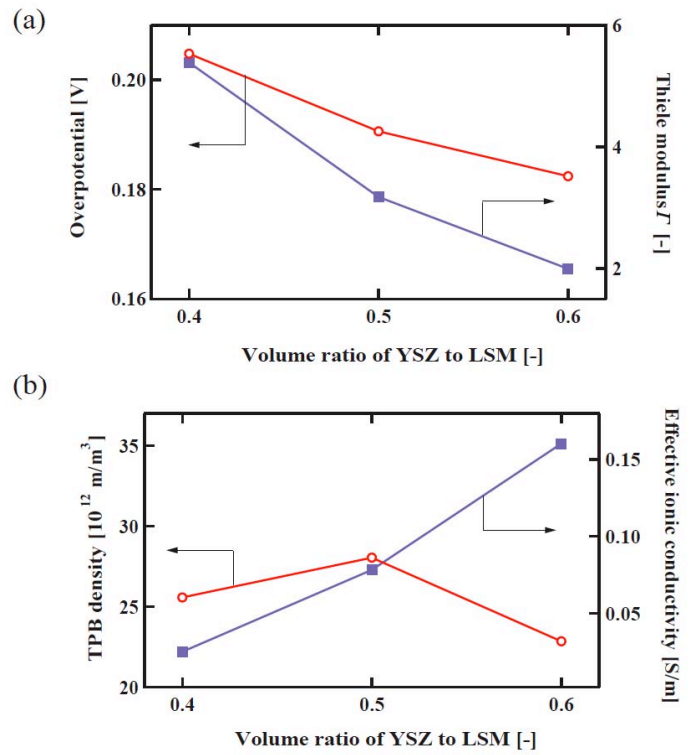


Fig. 16 The effects of volume fraction by RPM.

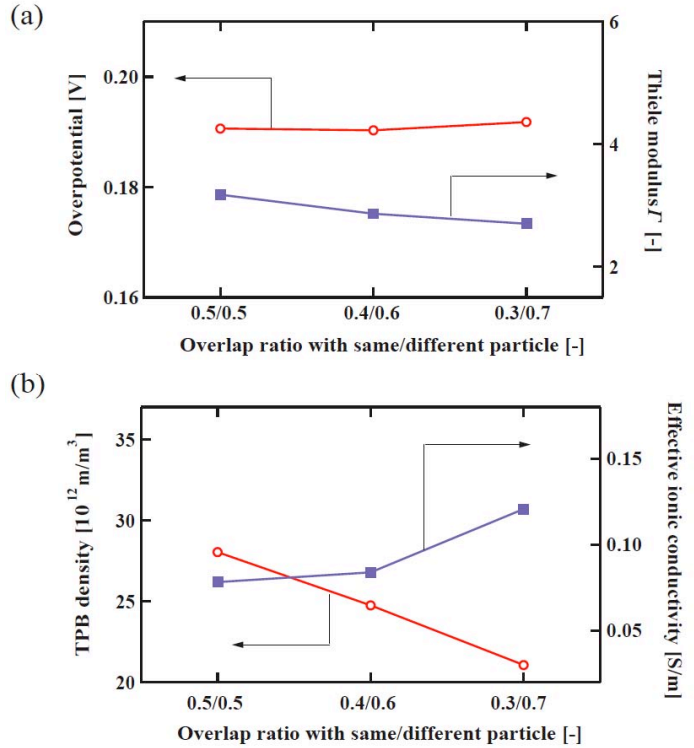
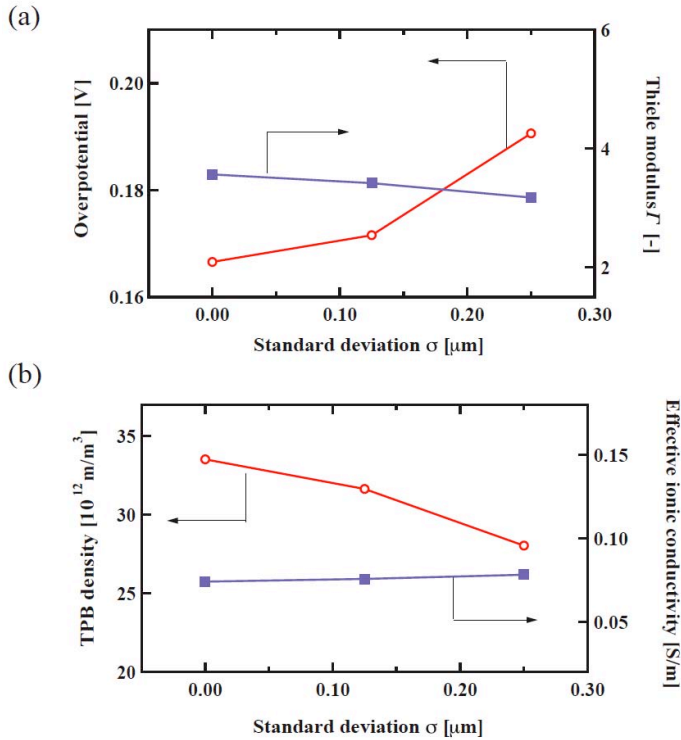


Fig. 17 The effects of overlap ratio by RPM.



**Fig. 18 The effects of particle size standard deviation by RPM.**

Predicted overpotentials from SR and RPM are compared in Fig. 14. It is noted that the overpotential value at the cathode-electrolyte interface corresponds to the overall overpotential. The overall overpotential of RPM is nearly 15 % larger than that of SR. It is considered that this agreement is good enough for the parametric survey of microstructures. This difference is attributed to the assumed sphere shape of RPM. The neck of the connected spherical YSZ particles makes effective ionic conductivity smaller than that in the SR method. This can be modified if other parameters that can express the actual neck connections in more detail.

The effects of the structural parameters on cathode overpotential are investigated using RPM. The predicted overpotential, Thiele modulus, three-phase boundary length and effective ionic conductivity are plotted against particle diameter in Fig. 15. The overpotential is reduced with smaller particles, which is caused by the increased TPB density. Figure 16 shows the effect of the volume fraction of ionic conductor (YSZ). The larger volume fraction of YSZ leads to smaller overpotential because of the increased ionic conductivity. Figure 17 shows the effect of overlap ratio. The overpotential is nearly independent of the overlap ratio, while the values of TPB density and the ionic conductivity are greatly affected. Figure 18 shows the effect of particle diameter standard deviation. The smaller  $\sigma$  results in smaller overpotential. This is because TPB density increases as standard deviation gets small.

## 5. CONCLUSION

The microstructures of the LSM/YSZ composite cathode were reconstructed using SR and RPM, and the 3-D electrochemical diffusion and conduction processes were solved by LBM. Following conclusions are obtained.

1. Clear images of the LSM/YSZ composite cathode can be obtained using the extremely low acceleration voltage SEM-EDX.
2. The cathode microstructures sintered at 1150, 1200, 1250 °C are well reconstructed using the SR method. The sintering-temperature dependence of overpotential in the electrochemical simulation agrees well with the experimental data.
3. From the parametric survey with RPM, it is shown that the smaller particle diameter, the smaller standard deviation of particle diameter and the larger YSZ volume ratio lead to the smaller overpotential. Due to the trade-off between TPB density and effective ionic conductivity, the total overpotential remains nearly unchanged against the overlap ratio.

## ACKNOWLEDGEMENTS

This research was supported through the 21<sup>st</sup> Century COE Program, "Mechanical System Innovation," by the Ministry of Education, Culture, Sports, Science and Technology of Japan (MEXT).

## NOMENCLATURE

|            |   |
|------------|---|
| $C$        | Molar concentration ( $\text{mol}/\text{m}^3$ )               |
| $c_i$      | Lattice velocity (m/s)  |
| $d$        | Particle diameter (m)   |
| $D$        | Diffusivity ( $\text{m}^2/\text{s}$ )                         |
| $F$        | Faraday constant: $9.649 \times 10^4$ (C/mol)                 |
| $f_i$      | Velocity distribution function (-)                            |
| $f_i^{eq}$ | Equilibrium velocity distribution function (-)                |
| $E$        | Evaluation function (-)                                       |
| $i$        | Phase (-)   |
| $i_0$      | Exchange current density at TPB ( $\text{A}/\text{m}^2$ )     |
| $i_{reac}$ | Exchange current density per volume ( $\text{A}/\text{m}^3$ ) |
| $I_N$      | Particle number (-)   |
| $L$        | Electrode length (m)  |
| $L_{TPB}$  | Density of three-phase boundary ( $\text{m}/\text{m}^3$ )     |
| $P$        | Pressure (Pa)   |
| $r$        | Distance (m)  |
| $R$        | Gas constant: 8.314 (J/mol K)                                 |
| $R_{ij}$   | Correlation function (-)                                      |
| $t$        | Time (s)  |
| $\Delta t$ | Unit step time (s)  |
| $w_i$      | Production in unit time (-)                                   |
| $T$        | Temperature (K)   |
| $x$        | Coordination (m)  |
| $Z$        | Phase function (-)  |

## Greeks

|                      |   |
|----------------------|---|
| $\alpha$             | Overlap ratio (-)                           |
| $\varepsilon$        | Volume fraction (-)                         |
| $\phi$               | Potential (V)                               |
| $\Gamma$             | Thiele modulus (-)                          |
| $\eta$               | Overpotential (V)                           |
| $\sigma$             | Standard deviation of particle diameter (m) |
| $\theta_a, \theta_c$ | Transfer coefficient (-)                    |
| $\tau$               | Tortuosity factor (-)                       |
| $\tau^*$             | Relaxation time (-)                         |

## Subscripts and superscript

|       |                 |
|-------|-----------------|
| $eff$ | Effective value |
| $el$  | Electron        |
| $io$  | Ion             |
| $O_2$ | Oxygen          |

## REFERENCES

- [1] Wilson, J. R. *et al.*, 2006, "Three-dimensional reconstruction of a solid-oxide fuel-cell anode," *Nature materials*, **5**, pp.541-544.
- [2] Koyama, M. *et al.*, 2007, "Development of Three-Dimensional Porous Structure Simulator for Optimizing Microstructure of SOFC Anode," *Proc. SOFC-X*, pp. 2057-2064.
- [3] Suzue, Y., Shikazono, N. and Kasagi, N., 2007, "Modeling of SOFC Anodes Based on the Stochastic Reconstruction Scheme," *Proc. SOFC-X*, pp. 2049-2055.
- [4] Yeong, C. L. Y. and Torquato, S., 1998, "Reconstructing random media. II. Three-dimensional media from two-dimensional cuts," *Phys. Rev. E*, **58** (1), pp. 224-233.
- [5] Asinari, P. *et al.*, 2007, "Direct numerical calculation of the kinematic tortuosity of reactive mixture flow in the anode layer of solid oxide fuel cells by the lattice Boltzmann method," *J. Power Sources*, **170**, pp. 395-375.
- [6] Joshi, A. S. *et al.*, 2007, "Lattice Boltzmann method for multi-component, non-continuum mass diffusion," *J. Phys. D: Appl. Phys.*, **40**, pp. 7593-7600.
- [7] Sakamoto, Y., Shikazono, N. and Kasagi, N., 2008, "Effects of electrode microstructure on polarization characteristics of SOFC anode," *Proc. ASME FUELCELL2008*, To be presented.
- [8] Costamagna, P. and Honegger, K., 1998, "Modeling of Solid Oxide Heat Exchanger Integrated Stacks and Simulation at High Fuel Utilization," *J. Electrochem. Soc.*, **145** (11), pp. 3995-4007.
- [9] Costamagna, P., Dosta, P. and Arato, E., 1998, "Short Communication, Some more considerations on the optimization of cermet solid oxide fuel cell," *Electrochimica Acta*, **43** (8), pp. 967-972.
- [10] Radhakrishnan, R., Virkar, A. V. and Singhal, S. C., 2005, "Estimation of Charge-Transfer Resistivity of  $\text{La}_{0.8}\text{Sr}_{0.2}\text{MnO}_3$  on  $\text{Y}_{0.16}\text{Zr}_{0.84}\text{O}_2$  Electrolyte Using Patterned Electrodes," *J. Electrochem. Soc.*, **152** (1), pp. A210-A218.
- [11] Chan, S. H. and Xia, Z. T., 2001, "Anode Micro Model of Solid Oxide Fuel Cell," *J. Electrochem. Soc.*, **144** (4), pp. A388-A394.
- [12] Jeon, D. H., Nam, J. H. and Kim, C. J., 2006, "Microstructural Optimization of Anode-Supported Solid Oxide Fuel Cells by a Comprehensive Microscale Model," *J. Electrochem. Soc.*, **153** (2), pp. A406-A417.
- [13] Zeiser, T. *et al.*, 2001, "CFD-calculation of flow, dispersion and reaction in acatalyst filled tube by the lattice Boltzmann method," *Chem. Eng. Sci.*, **56**, pp. 1697-1704.
- [14] Song, H. S. *et al.*, 2006, "Influences of starting particulate materials on microstructural evolution and electrochemical activity of LSM-YSZ composite cathode for SOFC," *J. Electroceram.*, **17**, pp. 759-764.
- [15] Kim, J. D. *et al.*, 2001, "Characterization of LSM-YSZ composite electrode by ac impedance spectroscopy," *Solid State Ionics*, **143**, pp. 379-389.